

# Metal–Organic Frameworks of Cu(II) Constructed from Functionalized Ligands for High Capacity H<sub>2</sub> and CO<sub>2</sub> Gas Adsorption and Catalytic Studies

Mayank Gupta, Nabanita Chatterjee, Dinesh De, Ranajit Saha, Pratim Kumar Chattaraj,\* Clive L. Oliver,\* and Parimal K. Bharadwaj\*



Cite This: <https://dx.doi.org/10.1021/acs.inorgchem.9b03012>



Read Online

ACCESS |



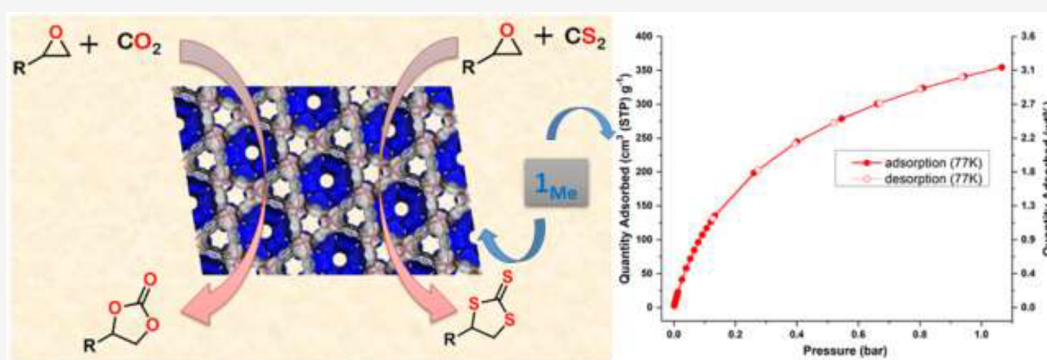
Metrics & More



Article Recommendations



Supporting Information



**ABSTRACT:** Two Cu(II)-based metal–organic frameworks (MOFs) having paddle-wheel secondary building units (SBUs), namely, **I<sub>Me</sub>** and **I<sub>ipr</sub>**, were synthesized solvothermally using two new bent di-isophthalate ligands incorporating different substituents. The MOFs showed high porosity (BET surface area, 2191 m<sup>2</sup>/g for **I<sub>Me</sub>** and 1402 m<sup>2</sup>/g for **I<sub>ipr</sub>**). For **I<sub>Me</sub>**, very high CO<sub>2</sub> adsorption (98.5 wt % at 195 K, 42.9 wt % at 273 K, 23.3 wt % at 298 K) at 1 bar was found, while for **I<sub>ipr</sub>**, it was significantly less (14.3 wt % at 298 K and 1 bar, 54.4 wt % at 298 K at 50 bar). **I<sub>Me</sub>** exhibited H<sub>2</sub> uptake of 3.2 wt % at 77 K and 1 bar of pressure, which compares well with other benchmark MOFs. For **I<sub>ipr</sub>**, the H<sub>2</sub> uptake was found to be 2.54 wt % under similar experimental conditions. The significant adsorption of H<sub>2</sub> and CO<sub>2</sub> for **I<sub>Me</sub>** could be due to the presence of micropores as well as unsaturated metal sites in these MOFs besides the presence of substituents that interact with the gas molecules. The experimental adsorption behavior of the MOFs could be justified by theoretical calculations. Additionally, catalytic conversions of CO<sub>2</sub> and CS<sub>2</sub> into useful chemicals like cyclic carbonates, cyclic trithiocarbonates, and cyclic dithiocarbonates could be achieved.

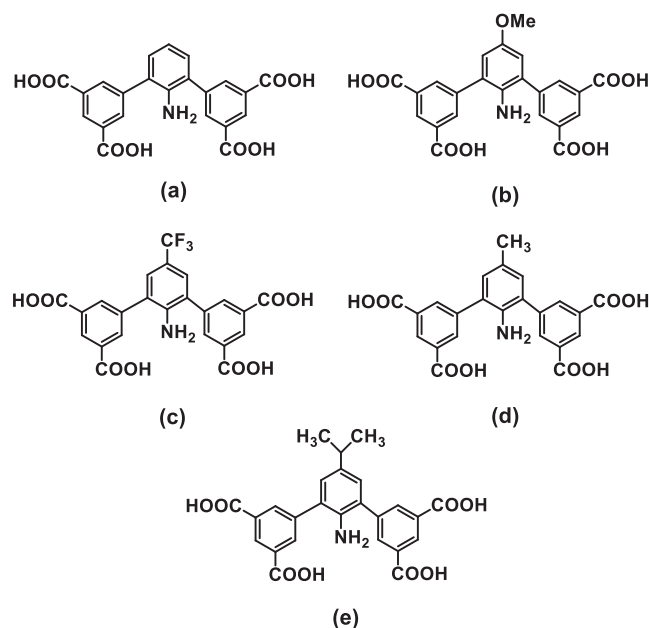
## INTRODUCTION

Metal–organic frameworks (MOFs) are an emerging class of hybrid porous materials. Due to their structural and functional tunability, easy synthesis, as well as their ever-expanding scopes of practical applications, MOFs have become one of the most pursued classes of materials.<sup>1</sup> The most important aspect is the fact that the overall structure and porosity in these materials can be systematically varied and fine-tuned through the choice of both metal ions and organic ligands.<sup>2</sup> Particularly, functionalization of MOFs with the polar functional group (NH<sub>2</sub>, NO<sub>2</sub>, Cl, Br, CO<sub>2</sub>H, OCH<sub>3</sub>, or SO<sub>3</sub>H)<sup>3</sup> enhances their adsorption performances for various gases (mainly H<sub>2</sub>, CO<sub>2</sub>, and CH<sub>4</sub>) besides developing their heterogeneous catalytic potential. The coordination space that can be rendered hydrophobic if alkyl or fluorinated (CH<sub>3</sub>, CF<sub>3</sub>) groups are present in the linkers could help in retaining gas adsorption efficiency even under moist conditions.<sup>4</sup>

Previously, we reported a porous Cu(II)-MOF built with the tetra-acid linker (Scheme 1a) that afforded a porous structure with paddle-wheel secondary building units (SBUs) and having free amine groups in the channels that exhibited a H<sub>2</sub> adsorption of 6.6 wt % at 77 K and 62 bar of pressure besides very high CO<sub>2</sub> adsorption (60 wt %) at 298 K.<sup>5</sup> Later on, the linker was modified with the introduction of OMe, CF<sub>3</sub>, and NH<sub>2</sub> groups on opposite sides of the central aromatic ring (Scheme 1b,c) to probe their possible influence in the gas adsorption behavior.<sup>6</sup> The Cu(II)-MOF with the linker shown in Scheme 1b afforded 34.2 wt % CO<sub>2</sub> at 273 K and negligible H<sub>2</sub> adsorption, while with the linker shown in Scheme 1c, it

Received: October 12, 2019

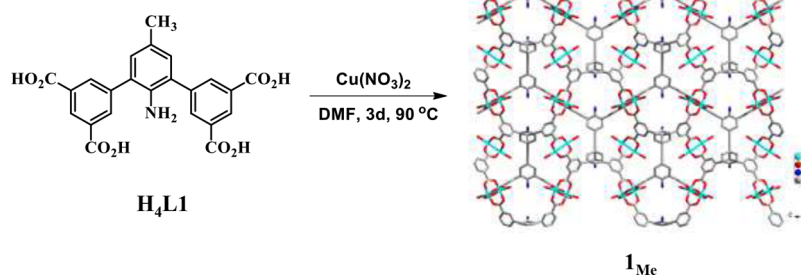
**Scheme 1. Schematic Diagram of Various Tetra-Acid Linkers**



exhibited 35.5 wt % CO<sub>2</sub> at 273 K and 1.72 wt % H<sub>2</sub> at 77 K and 1 bar of pressure. To probe the possible effects of electron donating methyl and isopropyl groups (Scheme 1d,e), the linkers H<sub>4</sub>L1 and H<sub>4</sub>L2 were synthesized and used to synthesize two Cu(II)-MOFs solvothermally. All the Cu(II)-MOFs built with the linkers shown in Scheme 1 were isostructural with copper paddle-wheel-based SBUs (Schemes 2 and 3) having highly porous and water stable architectures, allowing a comparative study of gas adsorption to be made. The significant adsorption of CO<sub>2</sub> and H<sub>2</sub> could be attributed to not only micropores and unsaturated metal sites formed in these MOFs but also enhanced interactions of functional groups with the gas molecules.<sup>7</sup>

Inspired by the excellent CO<sub>2</sub> sorption by the activated **I<sub>Me</sub>**, its usefulness as a heterogeneous catalyst in the cycloaddition reactions between various epoxides and CO<sub>2</sub> or CS<sub>2</sub> at 1.0 atm were probed. Catalytic conversion of carbon dioxide (CO<sub>2</sub>) and carbon disulfide (CS<sub>2</sub>) into useful chemicals like cyclic carbonates and cyclic tri- and dithiocarbonates is important for the effective utilization of harmful CO<sub>2</sub> and CS<sub>2</sub>.<sup>8</sup> The synthesis of cyclic carbonates by reacting an epoxide with CO<sub>2</sub> is a profitable reaction.<sup>9</sup> With the use of this reaction, this greenhouse gas can be reduced significantly. Also, the product cyclic carbonates in this reaction are useful in several industries

**Scheme 2. Synthesis of the MOF, **I<sub>Me</sub>****



like pharmaceuticals and dyes, as an electrolyte in Li<sup>+</sup> ion batteries, as polar aprotic solvents, as intermediates for the synthesis of ethylene glycol, as polymeric materials, as a precursor of polycarbonates, etc.<sup>10</sup> The cycloaddition products with CS<sub>2</sub>, e.g., dithiocarbonates and trithiocarbonates, are used in radioprotective studies,<sup>11</sup> polymer syntheses,<sup>12</sup> and making different insecticides.<sup>13</sup>

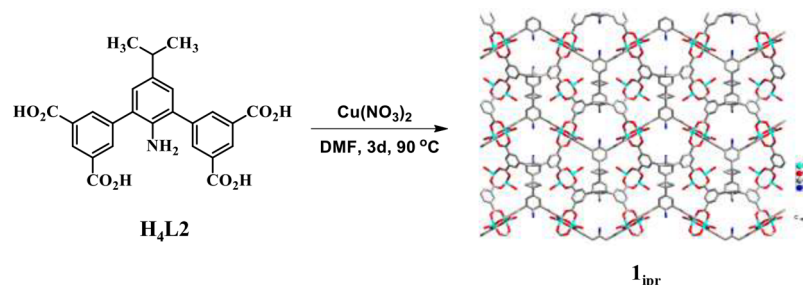
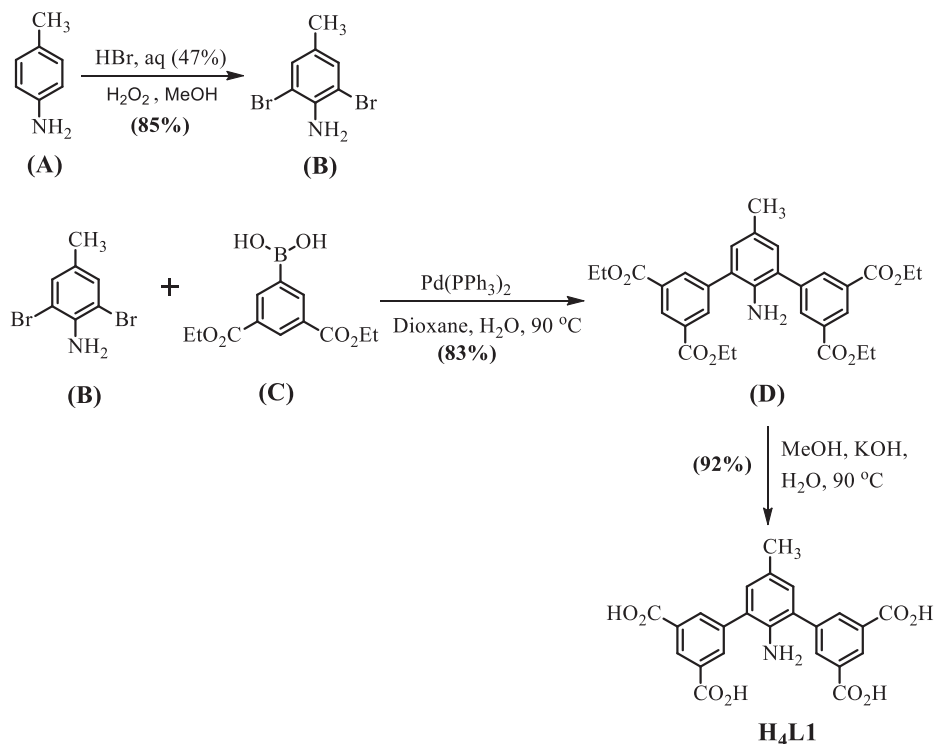
## EXPERIMENTAL SECTION

**Materials.** Cu(NO<sub>3</sub>)<sub>2</sub>·3H<sub>2</sub>O and other reagent grade chemicals were purchased from commercial suppliers (Sigma-Aldrich, Alfa Aesar, an TCI) and were used as received. All the solvents were acquired from S. D. Fine Chemicals, India. These solvents were purified following standard protocols prior to use.

**Physical Measurements.** All spectroscopic data were collected as described earlier.<sup>5</sup> Prior to the gas sorption analysis, the as-synthesized MOFs were kept in dry acetone and then heated at 120 °C under a high vacuum for 12 h to get rid of all the solvent molecules from the cavity. A Micromeritics 3Flex Surface Area Analyzer was used for all gas and water vapor sorption experiments. Sample preparation was achieved using a Micromeritics Flowprep with a constant flow of N<sub>2</sub> gas over the sample at 60 °C for 4 h. Afterward, the sample was heated first at 100 °C under a vacuum for 2 h followed by another hour of heating at 120 °C before the analysis commenced. The Brunauer–Emmett–Teller (BET) method was applied to data points with the slope of the Roquerol BET graph remaining positive.

**X-ray Structural Studies.** A Bruker SMART CCD diffractometer with graphite monochromated Mo K $\alpha$  radiation ( $\lambda = 0.71073 \text{ \AA}$ ) at 100 K was used for all data collections. The data collection, data reduction, structure solution, and refinements were carried out as described earlier.<sup>5</sup> The solvent molecules present in the structures were highly disordered. To tackle this, the PLATON-SQUEEZE<sup>14</sup> program was used and the number of solvent molecules calculated based on TGA and elemental analyses. The crystal data are shown in Table S1, and selected bond distances and angles are collected in Table S2.

**Computational Details.** We have analyzed the H<sub>2</sub> and CO<sub>2</sub> gas storage capacity of the synthesized MOFs in terms of the results from related computational studies. In order to reduce the computational cost, we have extracted and simplified the MOF structure from the associated experimental crystallographic data in such a way that all relevant interactions were kept intact. We studied the adsorption of H<sub>2</sub> and CO<sub>2</sub> gas molecules at different positions of the model complex. All of the structures were optimized using DFT-based  $\omega$ B97x-D<sup>15</sup> functional in conjunction with the TZVP basis set. Frequency calculations were done at the same level of theory on the optimized structures. All real frequency values ensured that the optimized structures were at the minima on their respective potential energy surfaces. The Gaussian 09 suite of program package<sup>16</sup> was used. The binding energy (BE) per gas molecule and Gibbs' free energy changes ( $\Delta G$ ) per gas molecule for both of the gas storage processes have been computed as

Scheme 3. Synthesis of the MOF, **1<sub>ipr</sub>**Scheme 4. Synthetic Route for the Ligand, **H<sub>4</sub>L1**

$$\text{BE} = \frac{1}{n}((nE_{\text{Gas}} + E_{\text{MOF}}) - E_{n\text{Gas@MOF}}) \quad (1)$$

$$\Delta G = \frac{1}{n}((nG_{\text{Gas}} + G_{\text{MOF}}) - G_{n\text{Gas@MOF}}) \quad (2)$$

where the  $E$  and  $G$  are the computed electronic energies and Gibbs' free energies of the optimized geometries respectively. The value of  $n$  is 21 for  $\text{H}_2$  and 12 for the  $\text{CO}_2$  gas adsorbed MOFs. The thermochemical parameters had been computed at 298 K temperature and 1 atm pressure.

The charge ( $q$ ) on each atomic center was computed by natural population analysis (NPA),<sup>17</sup> and the Wiberg bond index (WBI)<sup>18</sup> between two atoms was calculated as per the natural bond orbital (NBO) scheme<sup>19</sup> at the  $\omega\text{B97x-D/TZVP}$  level using NBO 3.1<sup>20</sup> as implemented in Gaussian 09. An ultrafine grid, with 99 radial shells per atom, and 950 angular points per shell, had been used throughout the computations.

The energy decomposition analysis (EDA)<sup>21</sup> was performed at the SSB-D<sup>22</sup>/TZP// $\omega\text{B97x-D/TZVP}$  level of theory using the ADF 2013.01 program package.<sup>23,24</sup> The SSB-D functional with Grimme's dispersion correction was reported to be suitable in representing weak interactions. In the EDA scheme, the interaction energy ( $\Delta E_{\text{int}}$ ) is decomposed into four energy terms, viz., the Pauli repulsion ( $\Delta E_{\text{pauli}}$ ), the electrostatic interaction energy ( $\Delta E_{\text{el}}$ ), the orbital interaction energy ( $\Delta E_{\text{orb}}$ ), and the dispersion interaction energy ( $\Delta E_{\text{disp}}$ ), as

$$\Delta E_{\text{int}} = \Delta E_{\text{pauli}} + \Delta E_{\text{el}} + \Delta E_{\text{orb}} + \Delta E_{\text{disp}} \quad (3)$$

The  $\Delta E_{\text{pauli}}$  represented the repulsion between the electrons having same spin in the occupied orbitals of the interacting fragments. The  $\Delta E_{\text{el}}$  term presented the quasi-classical electrostatic interaction energy between the fragments under consideration. In general, the  $\Delta E_{\text{el}}$  term was attractive in nature. Another attractive energy contribution was from the orbital interaction energy,  $\Delta E_{\text{orb}}$ , originating from the charge transfer, mixing of the occupied and unoccupied orbitals between the fragments, and the polarization effect. The term  $\Delta E_{\text{disp}}$  represented the dispersion energy correction toward the total attraction energy.

To analyze the nature of noncovalent interactions present in the  $\text{H}_2$  and  $\text{CO}_2$  adsorbed MOFs, an atoms-in-molecules (AIM)<sup>25</sup> analysis had been performed. Several density based parameters were computed at the  $\omega\text{B97x-D/TZVP}$  level of theory to find out the nature of the interactions. These calculations were done using Multiwfn software.<sup>26</sup>

The NCIPLOT software<sup>27,28</sup> was used to evaluate the noncovalent interactions between the guest gas molecules and the host MOF. The NCI analysis was based on the electron density ( $\rho$ ) and its reduced density gradient ( $s$ ) as

$$s = \frac{1}{2(3\pi^2)^{1/3}} \frac{|\nabla\rho|}{\rho^{4/3}} \quad (4)$$

where  $\nabla\rho$  is the gradient of  $\rho$ .

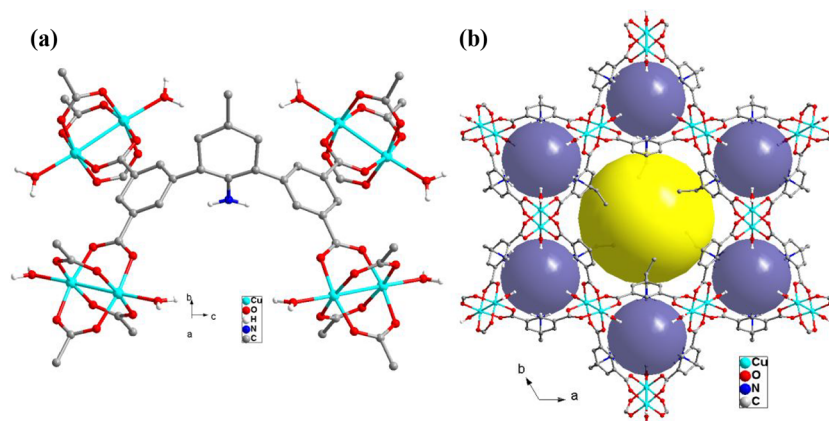


**Figure 1.** (a) Coordination environment around  $\text{Cu}^{2+}$  ions in  $\mathbf{1}_{\text{Me}}$  and (b) spherical cages in  $\mathbf{1}_{\text{Me}}$ .

A weak, noncovalent interaction between the molecular pairs could be identified by the low  $\rho$  and low  $s$  values. The Laplacian of electron density ( $\nabla^2\rho(r)$ ) was a parameter for describing the nature of the interaction between the molecular pairs. But, the  $\nabla^2\rho(r)$  index solely could not distinguish between different types of noncovalent interactions (hydrogen bonds, steric interactions, van der Waals' (vdW) interactions) by itself. The eigenvalues  $\lambda_i$  of the electron density Hessian (second derivative) matrix such that  $\nabla^2\rho(r) = \lambda_1 + \lambda_2 + \lambda_3$  ( $\lambda_1 < \lambda_2 < \lambda_3$ ) were useful to identify various noncovalent interactions. As for H bonds,  $\lambda_2 < 0$ ; for steric interactions,  $\lambda_2 > 0$ , and for vdW type of interactions,  $\lambda_2 \lesssim 0$ . Thus,  $s$  was plotted against  $\text{sign}(\lambda_2)\rho(r)$  (product of  $\text{sign}(\lambda_2)$  and  $\rho(r)$ ). The positions of the troughs associated with the reduced density gradient ( $s(\rho(r))$ ) appearing in the 2D plot give an idea about the type of the noncovalent interaction. The real space intermolecular interaction isosurface was generated using VMD visualization package.<sup>29</sup>

## SYNTHESIS

**Synthesis of the Ligand 2'-Amino-5'-methyl-[1,1':3',1''-terphenyl]-3,3'',5,5''-tetracarboxylic Acid ( $\mathbf{H}_4\mathbf{L1}$ ).** Synthesis of the ligand  $\mathbf{H}_4\mathbf{L1}$  was completed in several steps following a published procedure,<sup>1b</sup> as illustrated in Scheme 4. The precursor 2'-amino-5'-methyl-[1,1':3',1''-terphenyl]-3,3'',5,5''-tetracarboxylic ester ( $\mathbf{H}_4\mathbf{L1}$  ester) was characterized by X-ray crystallography (Figure S4), with Table S3 showing the crystal and refinement data.

**Synthesis of the Ligand 2'-amino-5'-isopropyl-[1,1':3',1''-terphenyl]-3,3'',5,5''-tetracarboxylic Acid ( $\mathbf{H}_4\mathbf{L2}$ ).** Synthesis of the ligand  $\mathbf{H}_4\mathbf{L2}$  was likewise completed in multiple steps following a similar procedure as above using *p*-isopropyl aniline in place of *p*-methyl aniline (Scheme S2). Synthetic details for  $\mathbf{H}_4\mathbf{L1}$  and  $\mathbf{H}_4\mathbf{L2}$  are provided in the Supporting Information.

**Synthesis of  $\{[\text{Cu}_2(\mathbf{L1})(\text{H}_2\text{O})_2] \cdot (6\text{DMF})(3\text{H}_2\text{O})\}_n$  ( $\mathbf{1}_{\text{Me}}$ ).** A solution of  $\text{Cu}(\text{NO}_3)_2 \cdot 3\text{H}_2\text{O}$  (22 mg, 0.092 mmol) and  $\mathbf{H}_4\mathbf{L1}$  (20 mg, 0.046 mmol) in 2 mL of DMF and 1 mL of  $\text{H}_2\text{O}$  was placed in a Teflon-lined stainless steel autoclave. It was heated under autogenous pressure to 90 °C for 3 days and then allowed to cool to room temperature. Blue crystals of  $\mathbf{1}_{\text{Me}}$  in the form of rectangular parallelepipeds were filtered, washed with DMF followed by methanol, and finally dried in the air. Yield ~ 23 mg (45%), based on the ligand  $\mathbf{H}_4\mathbf{L1}$ . FTIR (KBr pellets;  $\text{cm}^{-1}$ ): 3314 (b), 2920 (w), 1690 (m), 1630 (s), 1570 (s), 1467 (w), 1423 (s), 1365 (s), 919 (m), 863(w), 780 (m), 722 (m), 646 (m), 468 (m) (Figure S19a). Anal. Calcd for  $\text{C}_{41}\text{H}_{65}\text{N}_7\text{O}_{19}\text{Cu}_2$ : C, 45.29; H, 6.03; N, 9.01%. Found: C, 44.16; H, 6.41; N, 8.96%.

**Synthesis of  $\{[\text{Cu}_2(\mathbf{L2})(\text{H}_2\text{O})_2] \cdot (7\text{DMF})(2\text{H}_2\text{O})\}_n$  ( $\mathbf{1}_{\text{ipr}}$ ).** A similar procedure as above was followed using  $\mathbf{H}_4\mathbf{L2}$  (20 mg, 0.043 mmol) in lieu of  $\mathbf{H}_4\mathbf{L1}$ . Yield ~ 22 mg (43%), based on the ligand  $\mathbf{H}_4\mathbf{L2}$ . FTIR (KBr pellets;  $\text{cm}^{-1}$ ): 3443 (b), 2961 (w), 1655 (s), 1572(w), 1432(m), 1369 (s), 1250(w), 1230 (w) 1103 (w), 1069 (w) 922 (w), 783 (m), 727 (m), 657 (w), 482 (m) (Figure S19b). Anal. Calcd For

$\text{C}_{46}\text{H}_{74}\text{N}_8\text{O}_{19}\text{Cu}_2$ : C, 47.21; H, 6.37; N, 9.57%. Found: C, 46.30; H, 6.73; N, 9.49%.

**Thermal Stability and Activation of the Compounds,  $\mathbf{1}_{\text{Me}}$  and  $\mathbf{1}_{\text{ipr}}$ .** The bulk phase purity of the materials could be confirmed by matching their powder X-ray diffraction patterns (Figures S20 and S21) with those of crystallographically characterized samples. The thermogravimetric analysis showed a gradual loss of lattice solvent molecules from 50 °C onward, and decomposition of the compounds could be achieved only beyond 400 °C (Figure S22). The thermograms of the acetone exchanged samples exhibited a loss of solvent molecules up to 100 °C. Thereafter, no loss of weight could be observed up to 400 °C (Figures S23), suggesting robustness of the structures. High thermal stability of the compounds was also confirmed by the variable temperature PXRD measurements, showing the frameworks as stable at least up to 200 °C (Figures S20 and S21). Before gas sorption measurements and catalytic studies (for  $\mathbf{1}_{\text{Me}}$ ), the as-synthesized samples were activated as mentioned above to afford  $\mathbf{a1}_{\text{Me}}$  and  $\mathbf{a1}_{\text{ipr}}$ .

**General Procedure for the Cycloaddition of  $\text{CO}_2$  to Epoxides.** An epoxide (20 mmol), catalyst  $\mathbf{a1}_{\text{Me}}$  (10 wt %), and cocatalyst TBAB (1 mmol) were added to a Schlenk tube at room temperature with bubbling  $\text{CO}_2$  (99.999%). Once the reaction was completed as found by TLC, the catalyst was filtered out, washed with 5 mL of DCM, and air-dried. The product was purified by silica gel column chromatography and characterized by  $^1\text{H}$  NMR spectroscopy.

In a similar way, the conversion of atmospheric  $\text{CO}_2$  into cyclic carbonate was carried out. We purged the laboratory air as a  $\text{CO}_2$  source, and the mixture was allowed to stir for 24 h.

**General Procedure for the Synthesis of Cyclic Trithiocarbonates.** Carbon disulfide (40 mmol), an epoxide (20 mmol), catalyst  $\mathbf{a1}_{\text{Me}}$  (10 wt %), and cocatalyst TBAB (1 mmol) were placed in a sealed pressure tube and stirred at 0, 30, or 80 °C. After completion of the reaction, it was filtered, and the filtrate was evaporated off. The product was passed with a short plug of silica using ethyl acetate as the eluent and analyzed by  $^1\text{H}$  NMR spectroscopy.

## RESULTS AND DISCUSSION

Solvothermal reactions between  $\mathbf{H}_4\mathbf{L1}$  or  $\mathbf{H}_4\mathbf{L2}$  with  $\text{Cu}(\text{NO}_3)_2$  in the mixed solvent system of DMF and  $\text{H}_2\text{O}$  gave blue-colored crystals of  $\mathbf{1}_{\text{Me}}$  and  $\mathbf{1}_{\text{ipr}}$ , respectively. On the basis of single-crystal X-ray diffraction analysis in addition to thermal (TGA, Figures S22–24) and elemental analyses, these compounds were formulated as  $\{[\text{Cu}_2(\mathbf{L1})(\text{H}_2\text{O})_2] \cdot 6\text{DMF} \cdot 3\text{H}_2\text{O}\}_n$ ,  $\mathbf{1}_{\text{Me}}$ , and  $\{[\text{Cu}_2(\mathbf{L2})(\text{H}_2\text{O})_2] \cdot 7\text{DMF} \cdot 2\text{H}_2\text{O}\}_n$ ,  $\mathbf{1}_{\text{ipr}}$ . Both the compounds crystallized in the space group  $P6_3/mmc$  with the asymmetric unit comprising one-fourth of the ligand besides a  $\text{Cu}(\text{II})$  ion and a coordinated water molecule, each with half occupancy. As expected from an isophthalate moiety,

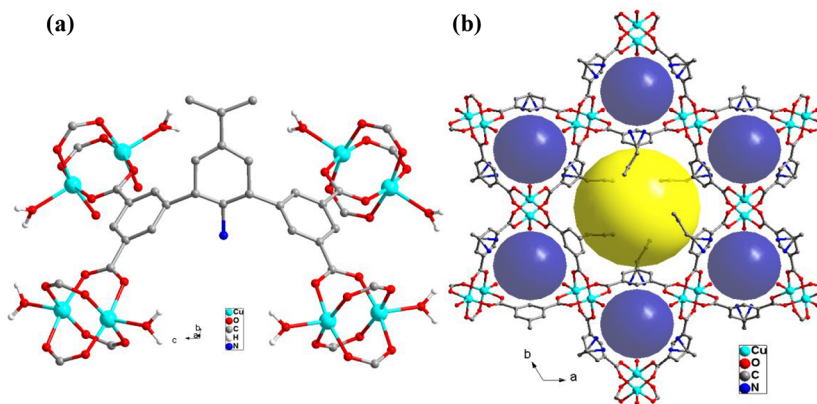


**Figure 2.** (a) Coordination environment around  $\text{Cu}^{2+}$  ions in  $\mathbf{1}_{\text{ipr}}$  and (b) spherical cages in  $\mathbf{1}_{\text{ipr}}$ .

the structure in  $\mathbf{1}_{\text{Me}}$  or  $\mathbf{1}_{\text{ipr}}$  was composed of paddle-wheel  $[\text{Cu}_2(\text{COO})_4]$  secondary building units (SBUs) with carboxylate bridging. (The  $\text{Cu}\cdots\text{Cu}$  bond distance was 2.650(3) and 2.6551(15) Å in  $\mathbf{1}_{\text{Me}}$  and  $\mathbf{1}_{\text{ipr}}$ , respectively; Figures 1a and 2a.) The  $\text{Cu}-\text{O}$  bond distances were in the range 1.949(6) to 2.087(11) Å for  $\mathbf{1}_{\text{Me}}$  and 1.950(6) to 2.124(6) Å for  $\mathbf{1}_{\text{ipr}}$ , forming an overall three-dimensional framework. These and other bond distances were within normal statistical errors as found in the literature. The overall structures of the present two compounds were quite similar to those with other linkers shown in Scheme 1. As depicted in Figures 1b and 2b, two types of voids of spherical shape were found with approximate diameters of 10 Å (yellow color) and 8 Å (violet color). These were further connected to each other via small triangular windows of dimensions  $\sim 5$  Å. The bigger void was in close proximity with the alkyl substituent, while the smaller void had  $-\text{NH}_2$  groups. Disordered solvent molecules occupied these voids whose number was established from the weight-loss in the thermogram, elemental, and IR spectral analyses. The sharp peaks at 1630 and 1655  $\text{cm}^{-1}$  in the IR spectra (Figure S19) of  $\mathbf{1}_{\text{Me}}$  and  $\mathbf{1}_{\text{ipr}}$ , respectively, were consistent with the  $\text{C}=\text{O}$  stretching vibration of the lattice DMF molecules. All these experimental data were in good agreement with the PLATON calculated solvent-accessible void volume, which was found to be 61.3% (4335/7068.2 Å<sup>3</sup>) for  $\mathbf{1}_{\text{Me}}$  and 57% (4037/7076.3 Å<sup>3</sup>) for  $\mathbf{1}_{\text{ipr}}$  of the total cell volume.

**Gas Adsorption Studies for  $\mathbf{1}_{\text{Me}}$ .** The permanent porosity in  $\mathbf{a1}_{\text{Me}}$  was established by nitrogen adsorption experiments at 77 K. As shown in Figure 3, it exhibited a reversible type I sorption behavior, revealing its microporous nature with a maximum  $\text{N}_2$  uptake of 568  $\text{cm}^3(\text{STP}) \text{g}^{-1}$  at 1 bar, corresponding to the BET surface area of 2191  $\text{m}^2\text{g}^{-1}$ .

The high permanent porosity, presence of open metal sites, and more importantly the presence of free amine/methyl groups prompted us to carry out  $\text{CO}_2$  adsorption measurements. We have carried out the measurements at different temperatures (Figure 4). The  $\text{CO}_2$  measurement results are summarized in Table 1.

The  $\text{CO}_2$  adsorption capacities of  $\mathbf{a1}_{\text{Me}}$  (Figure 4 and Table 1) at 195, 273, 278, 283, 288, 293, and 298 K were found to be 502  $\text{cm}^3 \text{g}^{-1}$  (98.5 wt %), 219  $\text{cm}^3 \text{g}^{-1}$  (42.9 wt %), 199  $\text{cm}^3 \text{g}^{-1}$  (39.0 wt %), 183  $\text{cm}^3 \text{g}^{-1}$  (35.8 wt %), 171  $\text{cm}^3 \text{g}^{-1}$  (33.6 wt %), 146  $\text{cm}^3 \text{g}^{-1}$  (28.7 wt %), and 119  $\text{cm}^3 \text{g}^{-1}$  (23.3 wt %), respectively. These high uptake capacities compared well with some of the MOFs known for  $\text{CO}_2$  adsorbing ability (Table S4). At zero loading, the  $Q_{\text{st}}$  value calculated using the

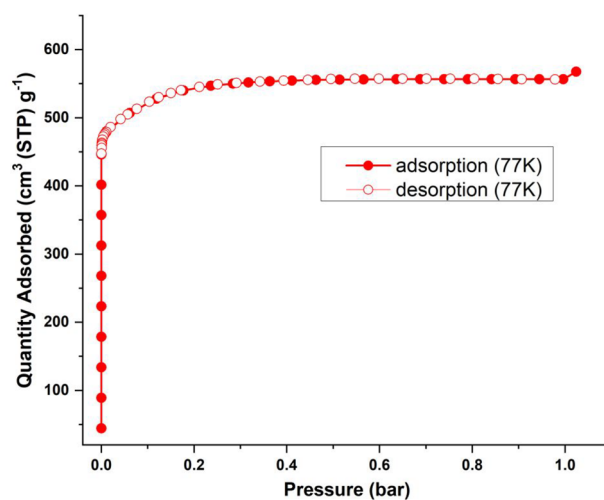


**Figure 3.**  $\text{N}_2$  physisorption isotherm of  $\mathbf{1}_{\text{Me}}$  at 77 K.

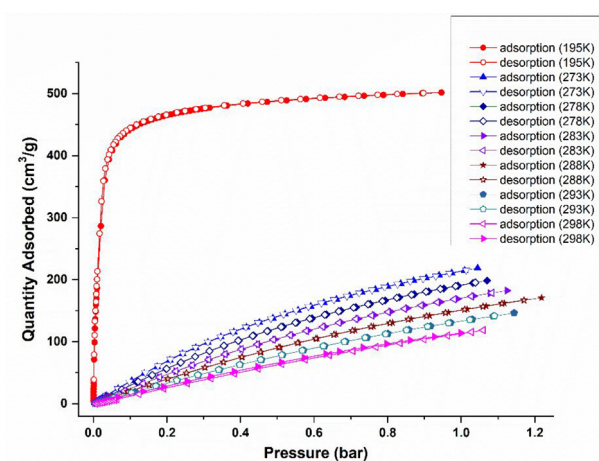


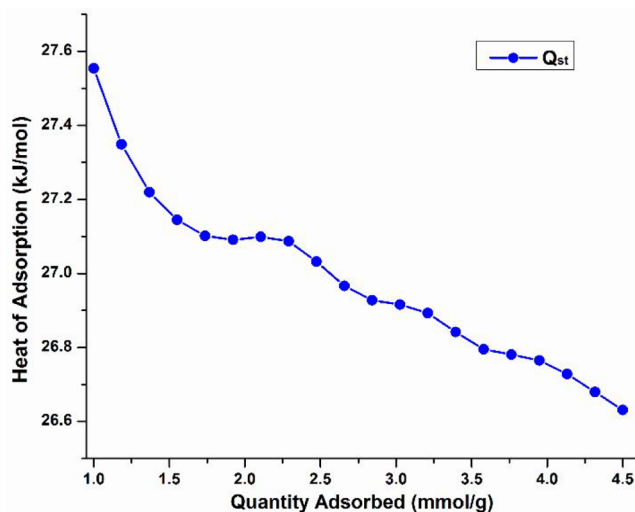
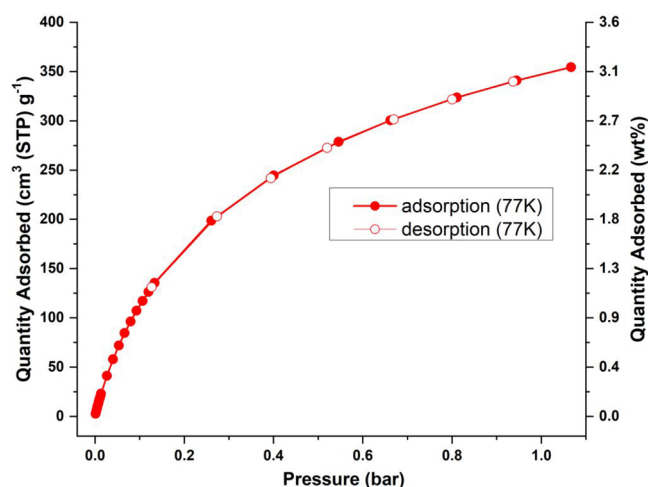
**Figure 4.** Physisorption isotherms:  $\text{CO}_2$  at 195 to 298 K for  $\mathbf{a1}_{\text{Me}}$ .

Clausius–Clapeyron equation was 26.63  $\text{kJ mol}^{-1}$ , indicative of a favorable interaction of  $\text{CO}_2$  with the host framework (Figure 5). For the process to calculate heat of  $\text{CO}_2$  adsorption from the Clausius–Clapeyron equation, see the SI.

The ability of  $\mathbf{a1}_{\text{Me}}$  to adsorb  $\text{H}_2$  gas at 77 K had also been carried out, with the results shown in Figure 6. The gas uptake reached about 355  $\text{cm}^3(\text{STP}) \text{g}^{-1}$ , corresponding to 3.2 wt % at a pressure of 1.07 bar. The adsorption and desorption follow

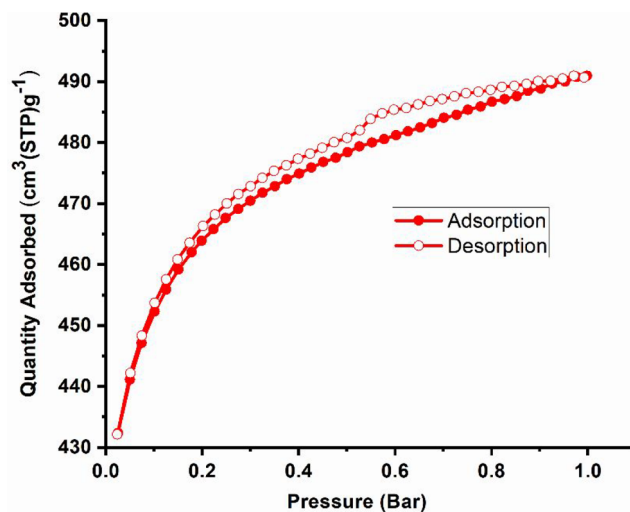
Table 1. CO<sub>2</sub> Gas Sorption Results for **1**<sub>Me</sub>

CO <sub>2</sub> , 195 K, 0.95 bar	502 cm <sup>3</sup> g <sup>-1</sup> (98.5 wt %)
CO <sub>2</sub> , 273 K, 1.04 bar	219 cm <sup>3</sup> g <sup>-1</sup> (42.9 wt %)
CO <sub>2</sub> , 278 K, 1.07 bar	199 cm <sup>3</sup> g <sup>-1</sup> (39.0 wt %)
CO <sub>2</sub> , 283 K, 1.12 bar	183 cm <sup>3</sup> g <sup>-1</sup> (35.8 wt %)
CO <sub>2</sub> , 288 K, 1.22 bar	171 cm <sup>3</sup> g <sup>-1</sup> (33.6 wt %)
CO <sub>2</sub> , 293 K, 1.14 bar	146 cm <sup>3</sup> g <sup>-1</sup> (28.7 wt %)
CO <sub>2</sub> , 298 K, 1.06 bar	119 cm <sup>3</sup> g <sup>-1</sup> (23.3 wt %)

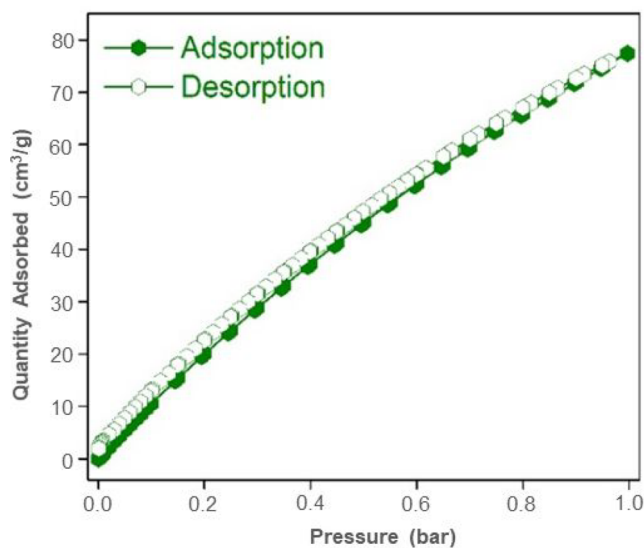
Figure 5. Isostatic heat of adsorption for CO<sub>2</sub> ( $Q_{st}$ ) for in **1**<sub>Me</sub>.Figure 6. Physorption isotherms: H<sub>2</sub> at 77 K (**1**<sub>Me</sub>).

the same path without hysteresis. Noticeably, the hydrogen uptake value was higher than those of MOF-5 (2.0%), MOF-505 (2.47%), Cu-BTT (2.42%), Fe-BTT (2.3%), PCN-68 (1.87%), PCN-66 (1.79%), SNU-4 (2.07%), MOF-74(Mg) (2.2%), and L<sub>Cu</sub> (2.57% and 1.72%) by Bharadwaj et al.<sup>30,6b</sup> and many among the NOTT measured at 1 bar of pressure (Table S5).

The structure of **1**<sub>ipr</sub> was isostructural with **1**<sub>Me</sub>. The only difference was **1**<sub>ipr</sub> had an isopropyl group in place of the methyl group. The permanent porosity in **1**<sub>ipr</sub> was established by N<sub>2</sub> adsorption experiments at 77 K. As shown in Figure 7, **1**<sub>ipr</sub> exhibited a maximum N<sub>2</sub> uptake of 491 cm<sup>3</sup> (STP) g<sup>-1</sup> at 1 bar, corresponding to the BET surface area of 1402 m<sup>2</sup>g<sup>-1</sup>.

Figure 7. Physorption isotherms: N<sub>2</sub> at 77 K for **1**<sub>ipr</sub>.

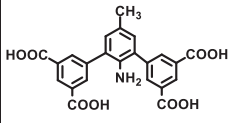
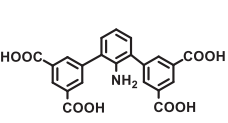
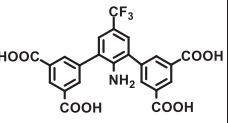
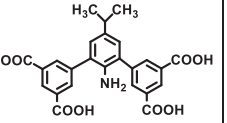
The CO<sub>2</sub> adsorption capacity of **1**<sub>ipr</sub> up to 1 bar of pressure (Figure 8) at 298 K was found to be 73 cm<sup>3</sup> (STP) g<sup>-1</sup> (14.3

Figure 8. Physorption isotherms: CO<sub>2</sub> at 298 K at 1 bar pressure for **1**<sub>ipr</sub>.

wt %), which was significantly less than the value obtained in the case of **1**<sub>Me</sub>. This could be attributed to the larger size of the isopropyl group compared to the methyl group reducing the available space.

We also compared the CO<sub>2</sub> gas sorption in isostructural MOFs at 298, 1 bar. When there is a methyl group, it is showing the highest uptake (119 cm<sup>3</sup> g<sup>-1</sup>), while when there is no group, the uptake was moderate (90 cm<sup>3</sup> g<sup>-1</sup>; Table 2). But when the methyl group is replaced by a trifluoromethyl group, the uptake was reduced to 106 cm<sup>3</sup> g<sup>-1</sup>. The trifluoromethyl group is electron withdrawing in nature, while the methyl group is electron donating, which increases the electron density at the amino group, leading to a favorable interaction with gas molecules. One should also notice that the trifluoromethyl group is bulkier than the methyl group, which can also lead to a decrease in gas sorption. But when the bulkier trifluoromethyl group was replaced by a smaller

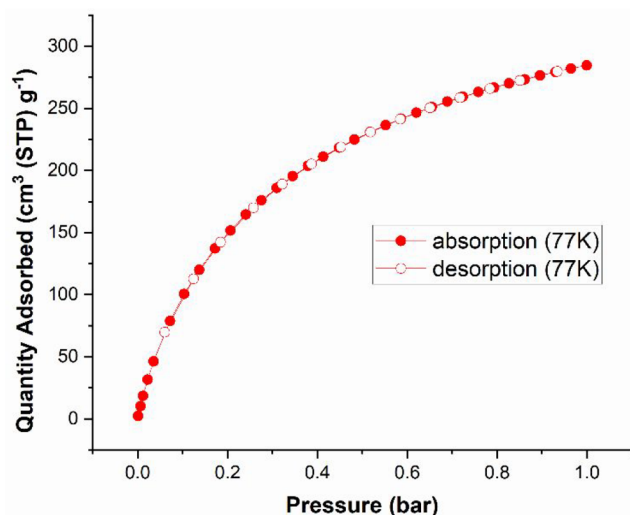
Table 2. Comparison of CO<sub>2</sub> Gas Sorption at 298 K, 1 Bar in Isostructural MOFs

MOF having ligand					
CO <sub>2</sub> uptake in cc/g (wt %)	119 (23.4 wt %)	90 (17.7 wt %)	106 (20.8 wt %)	73 (14.3 wt %)	106 (20.9 wt %)

fluoride group, no change in the gas sorption uptake was observed (Table 2). This shows that the size of the methyl group is appropriate at this pore size. The trifluoromethyl and fluoride groups showed more gas sorption when there was no group because of their favorable interactions with the gas molecule.

An attempt to increase the electron density at the amino group by replacing the methyl group with an isopropyl group leads to less gas uptake (73 cm<sup>3</sup> g<sup>-1</sup>). In this case, the bulkiness of the isopropyl group as compared to the methyl group causes inferior results. Hence, from the above observation, it can be concluded that the stereoelectronics are responsible for higher gas sorption.

The ability of **a1<sub>ipr</sub>** to adsorb H<sub>2</sub> gas at 298 K up to a pressure of 1 bar has also been carried out, and the results are shown in Figure 9. The gas uptake reaches about 284.6 cm<sup>3</sup> (STP) g<sup>-1</sup>, corresponding to 2.54 wt % up to a pressure of 1 bar.

Figure 9. Physisorption isotherms: H<sub>2</sub> at 77 K (**a1<sub>ipr</sub>**).

The gas adsorption selectivity for both the frameworks was measured<sup>31</sup> according to the ideal adsorbed solution theory (IAST) at 273 K up to 1 bar of pressure using single-component adsorption isotherms for CO<sub>2</sub>, H<sub>2</sub>, and N<sub>2</sub> (Figure 10). From the Figure, it was clear that the amounts of N<sub>2</sub> and H<sub>2</sub> uptake were negligibly small, whereas **a1<sub>Me</sub>** and **a1<sub>ipr</sub>** adsorbed significant amounts of CO<sub>2</sub>. For **a1<sub>Me</sub>**, the selectivity of CO<sub>2</sub> over N<sub>2</sub> was found to be 43, while it was 24 for **a1<sub>ipr</sub>**.

**Computational Study.** The optimized geometries of the MOFs and H<sub>2</sub> and CO<sub>2</sub> adsorbed MOFs presented in Figure 11 with the -CH<sub>3</sub>, -iPr, and -CF<sub>3</sub> substitution in the aromatic linker represented as **1<sub>Me</sub>**, **1<sub>ipr</sub>** and **1<sub>CF3</sub>**, respectively, in this study. The preferred binding sites for the H<sub>2</sub> gas

molecules in the paddle-wheel of the MOFs had been studied earlier and explained.<sup>32–34</sup> The H<sub>2</sub> molecules were placed in these preferred binding sites and optimized. Two H<sub>2</sub> molecules resided near each of the Cu atoms of the MOFs. The Cu–H bond lengths were in the range of 2.312–2.315 Å for all of the H<sub>2</sub> gas adsorbed MOFs. In these gas adsorbed MOFs, the H–H bond lengths of the two H<sub>2</sub> molecules close to the Cu atoms were elongated to 0.750 Å compared to 0.744 Å in the free H<sub>2</sub> molecule (see Table S6). The remaining H<sub>2</sub> molecules were distributed over the Cu-paddle and aromatic linkers. The elongation in the H–H bond was small in these H<sub>2</sub> molecules compared to free H<sub>2</sub> molecules (see Table S6). A similar type of scenario was present in case of the CO<sub>2</sub> adsorbed MOFs. Two Cu atoms were found to be bound with two CO<sub>2</sub> molecules showing Cu–O interactions. The Cu–O distances were in the range 2.403–2.425 Å for all of the MOFs (see Table S7). The C–O1 bond distance (1 referred to the O close to the Cu atom) in CO<sub>2</sub> was increased, whereas the other one (C–O2 bond) was shortened as compared to free CO<sub>2</sub>. For the remaining CO<sub>2</sub> molecules, the elongation was very small. The O1–C–O2 bond angle was bent in the adsorbed form for all CO<sub>2</sub> molecules. As we could see for the H<sub>2</sub> as well as for the CO<sub>2</sub> gas molecules, the change in the structural parameters was very small. Hence, physisorption of these gases was expected in the case of all the MOFs.

The binding energy per gas molecule (BE) and the Gibbs' free energy change per gas molecule ( $\Delta G$ , kcal/mol) were computed and are presented in Table S8. The BE values were the same for a particular gas in case of the **1<sub>Me</sub>**, as well as for the **1<sub>ipr</sub>** and **1<sub>CF3</sub>**. The H<sub>2</sub> and CO<sub>2</sub> storage capacity could be explained in terms of the  $\Delta G$  values. The  $\Delta G$  values for both of the CO<sub>2</sub> adsorbed MOFs were the same, which supports almost equal CO<sub>2</sub> storage capacity in the MOFs at 298.15 K and 1 atm. For the H<sub>2</sub> desorption process, the  $\Delta G$  value for **1<sub>Me</sub>** was -4.9 kcal/mol; for **1<sub>ipr</sub>**, -5.0 kcal/mol; and for **1<sub>CF3</sub>**, -5.1 kcal/mol. Thus, the high H<sub>2</sub> gas storage in **1<sub>Me</sub>** and **1<sub>ipr</sub>** as compared to the **1<sub>CF3</sub>** was thermochemically supported. The computational results were in conformity with those obtained from related experiments.

In the EDA scheme, we had considered three fragmentation processes as shown in Table S9. In the first scheme, two gas molecules near the two Cu centers were considered as one fragment, and the remaining part ( $n-2$ )gas@MOF was considered as the other fragment. In the second fragmentation process, we had considered the two nearby gas molecules near the Cu atoms and the MOF, i.e., 2gas@MOF, as one fragment, and the remaining ( $n-2$ ) gas molecules as another fragment. In the last fragmentation process, we had considered the MOF as one fragment and all of the  $n$  gas molecules as the second fragment. For all of the fragmentation processes, the contributions from the noncovalent interactions ( $\Delta E_{\text{elstat}} + \Delta E_{\text{disp}}$ ) were more than the covalent interaction ( $\Delta E_{\text{orb}}$ ). The two gas molecules near the Cu atoms were mainly stabilized by

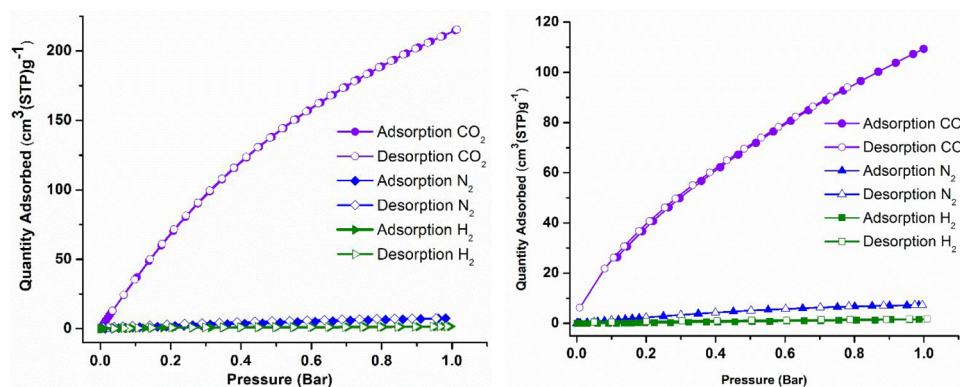


Figure 10. CO<sub>2</sub>, H<sub>2</sub>, and N<sub>2</sub> absorption isotherm for **1**<sub>Me</sub> (left) and **1**<sub>ipr</sub> (right) at 273 K.

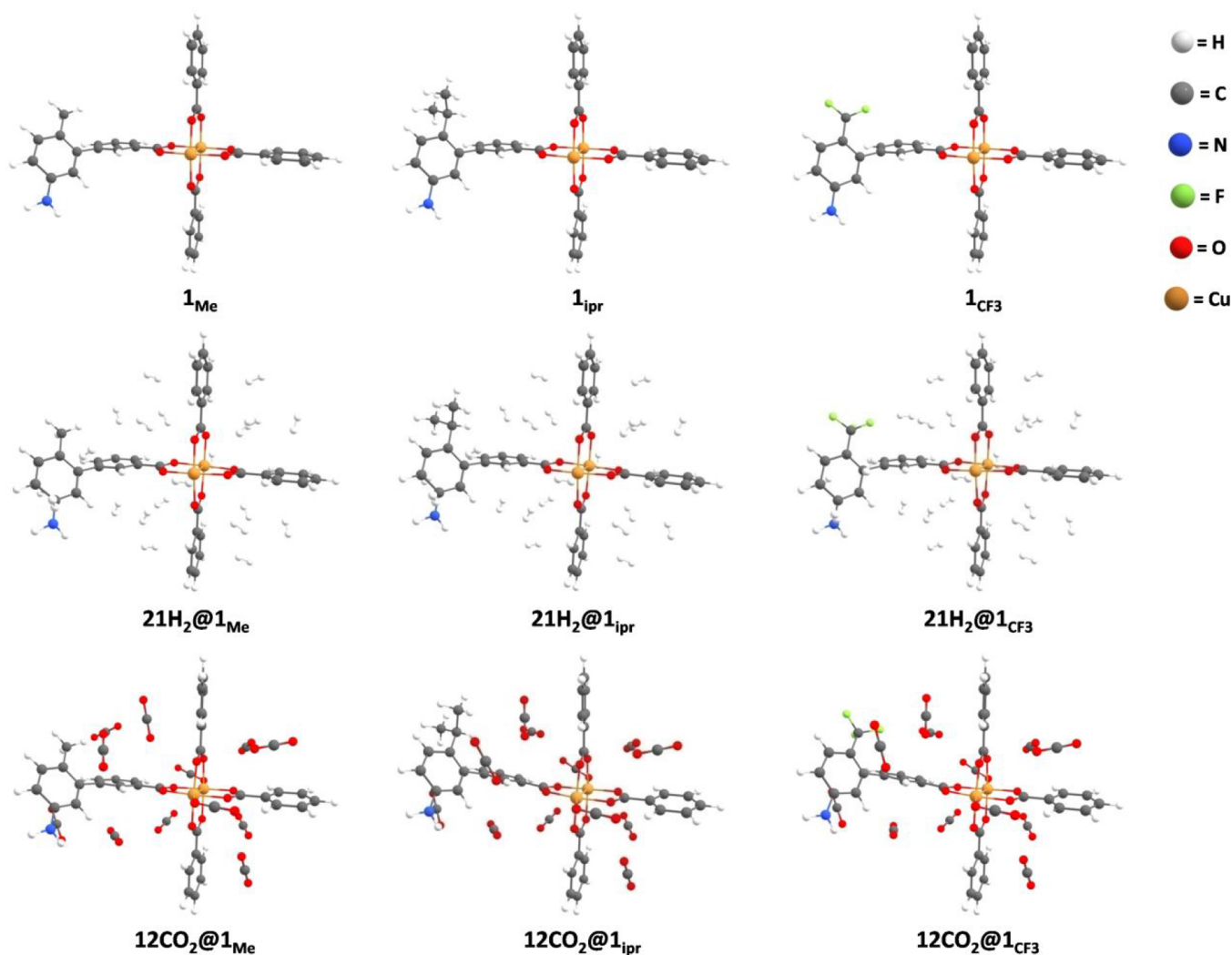
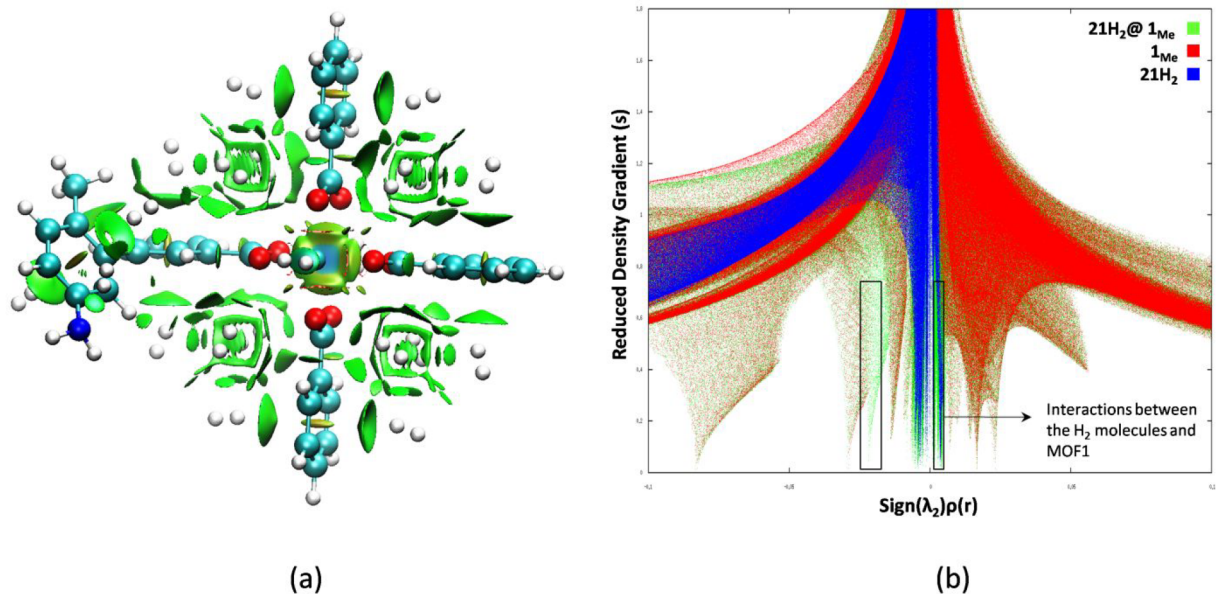


Figure 11. Optimized geometries of all the structures at the  $\omega$ B97x-D/TZVP level of theory.

the  $\Delta E_{\text{elstat}}$  (49.1–58.7%), which was followed by the  $\Delta E_{\text{orb}}$  (28.6–40.3%) and  $\Delta E_{\text{disp}}$  (10.5–17.7%) as per the first fragmentation way. For the remaining ( $n-2$ ) gas molecules, the  $\Delta E_{\text{disp}}$  contributes 42.0–45.4% toward the total stabilization energy, becoming the major stabilizing factor for these gas molecules as per the second fragmentation procedure. Overall, it was clear that the noncovalent interactions ( $\Delta E_{\text{elstat}}$  and

$\Delta E_{\text{disp}}$ ) were the major stabilizing factor compared to the  $\Delta E_{\text{orb}}$ .

The molecular graphs of the H<sub>2</sub> and CO<sub>2</sub> adsorbed MOFs had been generated at the  $\omega$ B97x-D/TZVP level and presented in Figure S25. Large numbers of bond paths cropped up between different atoms of the MOFs and gas molecules, indicating all of the interactions in these gas adsorbed MOF systems. The computed density based descriptors at the bond



**Figure 12.** Plot of (a) the NCI isosurface for  $21\text{H}_2@1_{\text{Me}}$ . The iso-surface is generated for  $s = 0.5$  au and (b) the reduced density gradient ( $s$ ) versus  $\text{sign}(\lambda_2)\rho$  for  $21\text{H}_2@1_{\text{Me}}$ .

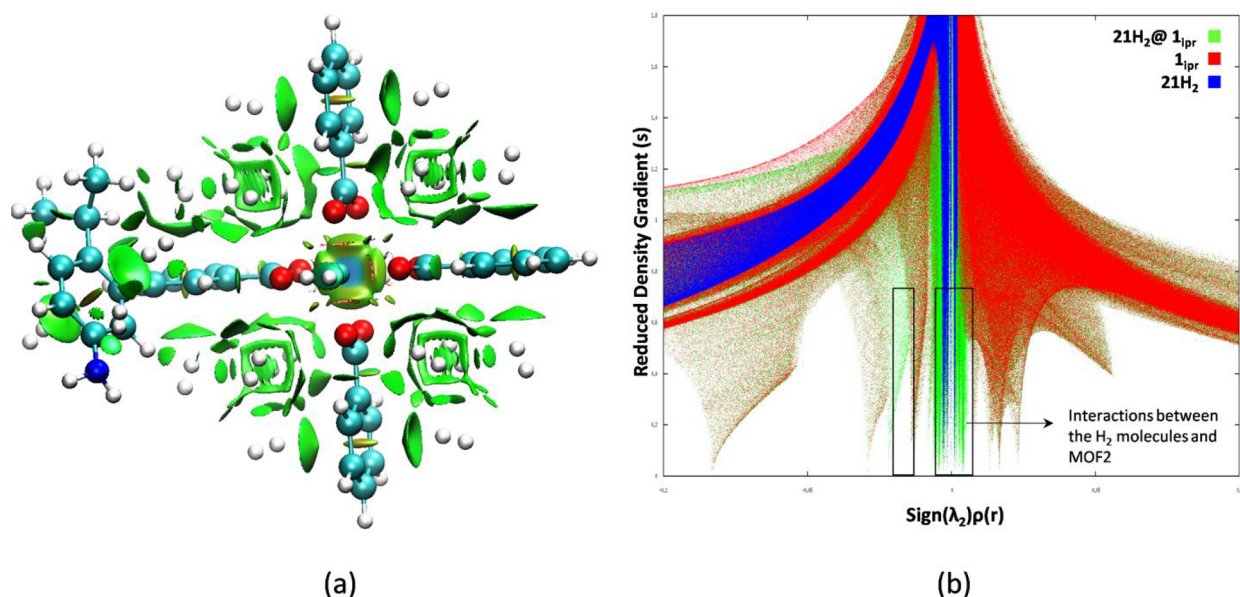


**Figure 13.** Plot of (a) the NCI isosurface for  $12\text{H}_2@1_{\text{ipr}}$ . The iso-surface is generated for  $s = 0.5$  au and (b) the reduced density gradient ( $s$ ) versus  $\text{sign}(\lambda_2)\rho$  for  $12\text{H}_2@1_{\text{ipr}}$ .

critical points (BCP) are presented in Table S10. We had considered only one of each kind of BCP for the discussion. The electron density ( $\rho(r_c)$ ) values were low at the BCPs originating between the adsorbed gas molecules and MOFs. The low  $\rho(r_c)$ , positive Laplacian of the electron density ( $\nabla^2\rho(r_c)$ ), and positive energy density ( $H(r_c)$ ) at the BCP indicated noncovalent type interactions present between the gas molecules and MOFs. The NCI plots for all of these gas adsorbed MOF systems have been presented in Figures 12, 13, S26, and S27. The generated green surface between the gas and MOFs surface indicated the origin of van der Waals interaction among them. The 2-D plot showed the generation of a green area near the electron density equal to zero, indicating all of the interactions between the MOF surface and

gas molecules. The  $\text{H}_2$  and  $\text{CO}_2$  near the Cu atom had their finger prints near the region of  $\text{sign}(\lambda_2)\rho(r) \approx -0.021$  to  $-0.028$ , which almost coincided with the Cu–Cu interaction in the paddle-wheel.

The results obtained from the NBO analysis for the  $\text{H}_2$  and  $\text{CO}_2$  adsorbed MOF systems have been presented in Table S11 and Table S12, respectively. The charges on the Cu atoms in  $1_{\text{Me}}$  are 1.093 and 1.094 |e|, in  $1_{\text{ipr}}$  are 1.093 and 1.094 |e|, and in  $1_{\text{CF}_3}$  are 1.093 and 1.093 |e|. On  $\text{H}_2$  adsorption, the charges on the Cu atoms decreased to 1.045 for  $1_{\text{Me}}$ , 1.045 for  $1_{\text{ipr}}$ , and 1.046 and 1.045 for  $1_{\text{CF}_3}$ . The two  $\text{H}_2$  molecules near the Cu atoms had a positive charge on them. This signified a transfer of electron density from the  $\text{H}_2$  molecules to the Cu centers. The remaining  $\text{H}_2$  molecules in the vicinity of the

aromatic linkers were polarized, which was the origin of the vdW force. The total charges on the two CO<sub>2</sub> molecules near the two Cu atoms were 0.048 and 0.044 lel in 12CO<sub>2</sub>@**1**<sub>Me</sub> and 0.045 and 0.044 lel in 12CO<sub>2</sub>@**1**<sub>ipr</sub> and 0.046 and 0.044 lel in 12CO<sub>2</sub>@**1**<sub>CF<sub>3</sub></sub>, respectively. This accumulation of positive charge on CO<sub>2</sub> with a concomitant decrease of the charge on both the Cu atoms indicated that electron density donation occurred from CO<sub>2</sub> toward the MOFs. The remaining 10 CO<sub>2</sub> molecules were polarized. The Cu–H and Cu–O(CO<sub>2</sub>) WBI values were low, supporting the noncovalent type of interactions. The WBI<sub>H–H</sub> values in the adsorbed H<sub>2</sub> molecules were slightly smaller compared to those in the free H<sub>2</sub> molecules. A similar picture was found for the WBI<sub>C–O</sub> in the adsorbed CO<sub>2</sub> molecules.

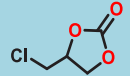
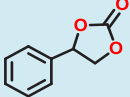
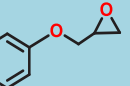
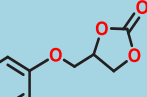
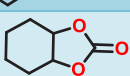
**Catalytic Studies. Cycloaddition of CO<sub>2</sub> to Different Epoxides.** High CO<sub>2</sub> adsorption ability with significant heat of adsorption for **a1**<sub>Me</sub> convinced us to attempt to fix adsorbed CO<sub>2</sub> as cyclic carbonates by reacting with different epoxides. In a typical experiment, an epoxide (20 mmol), catalyst **a1**<sub>Me</sub> (10 wt %), and cocatalyst TBAB (1 mmol) were placed in a Schlenk tube with stirring at room temperature, and CO<sub>2</sub> (99.999%) was allowed to bubble into the reaction mixture. The catalyst system was quite versatile, as structurally different epoxides could be converted to the corresponding cyclic carbonates in excellent yields (Table 3).

To confirm the heterogeneous nature of the reaction, a hot filtration technique was adopted. The reaction using epichlorohydrin as the substrate was stopped by hot filtration of the catalyst at partial conversion (~50%) after dilution with

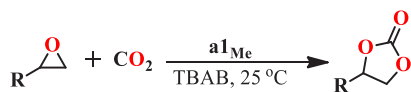
dichloromethane. No further reaction occurred when the filtrate was allowed to react under the same reaction conditions (Figure S28). To check the reusability of the catalyst, it was collected by filtration, washed with CH<sub>2</sub>Cl<sub>2</sub>, and dried under a vacuum at 120 °C for 5 h and used for the second run using the same reactants. The catalyst could be reused without any noticeable loss of activity (Figure S29) and crystallinity (Figure S30) at least up to four cycles. The yields in four runs were almost the same. Formation of the desired carbonate was confirmed by its <sup>1</sup>H NMR (Figures S31–S35). High yields of the desired products in these reactions under mild conditions may be due to high accessibility of the empty Cu(II) coordination sites where an epoxide could easily bind.

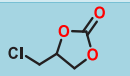
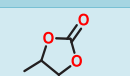
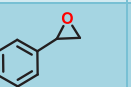
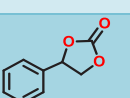
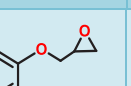
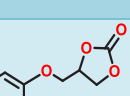
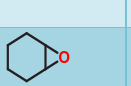
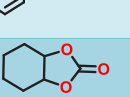
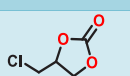
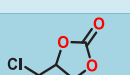
We then attempted bubbling of laboratory air into the reaction mixture of an epoxide, TBAB, and the catalyst **a1**<sub>Me</sub>, taken in the same proportion as above for 24 h at room temperature. The results were quite interesting (Table 4), and a significant amount of the product could be isolated this way.

**Table 4. Cycloaddition Reactions by Bubbling Laboratory Air for 24 h into the Reaction Mixture at 298 K**

Entry	Epoxide	Product	Conversion %
1			65
2			50
3			60
4			35

**Table 3. Cycloaddition of CO<sub>2</sub> and Various Epoxides Catalyzed by **a1**<sub>Me</sub> in the Presence of TBAB<sup>a</sup>**



Entry	Epoxide	Product	Time(h)	Conversion %
1			12	>99
2			12	>99
3			12	>99
4			12	94
5			22	84
6			32	4 <sup>a</sup>
7			32	9 <sup>b</sup>

<sup>a</sup>Catalyzed by **1**<sub>Me</sub> only. <sup>b</sup>Catalyzed by the cocatalyst TBAB alone.

**Cycloaddition of CS<sub>2</sub> to Epoxides.** We next attempted to catalyze the reaction between an epoxide and CS<sub>2</sub> in the presence of **1**<sub>Me</sub>. The reaction was performed in a sealed pressure tube using an epoxide (20 mmol), CS<sub>2</sub> (40 mmol), catalyst **a1**<sub>Me</sub> (10 wt %), and the cocatalyst TBAB (1 mmol) at different temperatures under solvent free conditions. At 0 °C, after 12 h, two major products could be isolated after purification through silica chromatography and characterized as a mixture of cyclic dithiocarbonate and trithiocarbonate through <sup>1</sup>H NMR. On increasing the temperature to 30 °C, still the mixture was obtained. On further increasing the temperature to 80 °C, thin-layer chromatography (TLC) showed a single major spot, which was passed through a short plug of silica using CH<sub>2</sub>Cl<sub>2</sub> as an eluent and characterized by <sup>1</sup>H NMR (Figures S36–S40) and matched with the reported literature,<sup>35</sup> which confirmed the formation of exclusive cyclic trithiocarbonate (Table 5). In some cases, crystals appeared after some time. X-ray structure data were also collected for those crystals, which confirmed the presence of cyclic trithiocarbonate (Figure S41). The probable mechanism<sup>28a</sup> is provided in Figure S42. A heterogeneous nature (Figure S43) and recyclability (Figures S44 and S45) were also confirmed as in the case of cyclic carbonates.

**Table 5. Cycloaddition of CS<sub>2</sub> and Various Epoxides Catalyzed by **1**<sub>Me</sub>**



Entry	Epoxide	Product	Time(h)	Conversion %
1			12	70
2			12	63
3			12	69
4			12	65
5			12	40

## CONCLUSIONS

Two 3D Cu(II)-MOFs were synthesized solvothermally with two new tetra-acid ligands and characterized by single crystal X-ray diffraction. Each structure had a metal-bound aqua ligand in addition to a number of solvent molecules in the voids. All these could be removed upon heating without a breakdown of the 3D architecture, leading to highly porous structures. The amino group remained uncoordinated in the voids, which along with uncoordinated metal centers exhibited very high H<sub>2</sub> and CO<sub>2</sub> adsorption by the MOFs. With activated **1**<sub>Me</sub>, the adsorbed CO<sub>2</sub> could be easily fixed as a cyclic carbonate on reacting with an epoxide at room temperature in the presence of TBAB as the cocatalyst. Even CO<sub>2</sub> from laboratory air could be fixed this way. Conversion of carbondisulfide (CS<sub>2</sub>) into cyclic trithiocarbonates was also achieved using **1**<sub>Me</sub>. Theoretical calculations supported high uptake capacity for CO<sub>2</sub> and H<sub>2</sub>.

## ASSOCIATED CONTENT

### Supporting Information

The Supporting Information is available free of charge at <https://pubs.acs.org/doi/10.1021/acs.inorgchem.9b03012>.

X-ray crystallographic data of **1**<sub>Me</sub> (CCDC 1896029), **1**<sub>ipr</sub> (CCDC 1896030), H<sub>4</sub>L1 ester (CCDC 1896027), and H<sub>4</sub>L2 ester (CCDC 1896028); ESI-MS spectra; IR spectra; TGA, PXRD, and NMR spectra (PDF)

### Accession Codes

CCDC 1896027–1896030 contain the supplementary crystallographic data for this paper. These data can be obtained free of charge via [www.ccdc.cam.ac.uk/data\\_request/cif](http://www.ccdc.cam.ac.uk/data_request/cif), or by emailing [data\\_request@ccdc.cam.ac.uk](mailto:data_request@ccdc.cam.ac.uk), or by contacting The Cambridge Crystallographic Data Centre, 12 Union Road, Cambridge CB2 1EZ, UK; fax: +44 1223 336033.

## AUTHOR INFORMATION

### Corresponding Authors

Pratim Kumar Chattaraj – Department of Chemistry and Center for Theoretical Studies, Indian Institute of Technology

Kharagpur, Kharagpur 721302, India; Email: [pkc@chem.iitkgp.ac.in](mailto:pkc@chem.iitkgp.ac.in)

Clive L. Oliver – Centre for Supramolecular Chemistry Research (CSCR), Department of Chemistry, University of Cape Town, Cape Town, South Africa; [orcid.org/0000-0001-7946-6492](https://orcid.org/0000-0001-7946-6492); Email: [clive.oliver@uct.ac.za](mailto:clive.oliver@uct.ac.za)

Parimal K. Bhadraraj – Department of Chemistry, Indian Institute of Technology Kanpur, Kanpur 208016, India; Department of Chemistry, Indian Institute of Technology Bombay, Mumbai 400076, India; [orcid.org/0000-0003-3347-8791](https://orcid.org/0000-0003-3347-8791); Email: [pkb@iitk.ac.in](mailto:pkb@iitk.ac.in)

### Other Authors

Mayank Gupta – Department of Chemistry, Indian Institute of Technology Kanpur, Kanpur 208016, India

Nabanita Chatterjee – Centre for Supramolecular Chemistry Research (CSCR), Department of Chemistry, University of Cape Town, Cape Town, South Africa

Dinesh De – Department of Basic Science, Vishwavidyalaya Engineering College, Lakhanpur, Sarguja University, Lakhanpur 497116, India

Ranajit Saha – Department of Chemistry and Center for Theoretical Studies, Indian Institute of Technology Kharagpur, Kharagpur 721302, India

Complete contact information is available at:

<https://pubs.acs.org/10.1021/acs.inorgchem.9b03012>

### Notes

The authors declare no competing financial interest.

## ACKNOWLEDGMENTS

We gratefully acknowledge the financial support received from the DST and MNRE, New Delhi, India (to P.K.B.) and SRF from the University Grants Commission (UGC), New Delhi, India to M.G. D.D. thanks “TEQIP Collaborative Research Scheme (CRS).” R.S. and P.K.C. thank UGC and DST, New Delhi, for Ph.D. and J. C. Bose fellowships, respectively.

## REFERENCES

- (1) Eddaoudi, M.; Kim, J.; Rosi, N.; Vodak, D.; Wachter, J.; O’Keeffe, M.; Yaghi, O. M. Systematic Design of Pore Size and Functionality in Isoreticular MOFs and Their Application in Methane Storage. *Science* **2002**, *295*, 469–472. (b) Gupta, M.; Kottlilil, D.; Tomar, K.; Lu, S.; Vijayan, C.; Ji, W.; Bhadraraj, P. K. Two-Photon Absorption and Fluorescence in Micrometer-Sized Single Crystals of a Rhodamine B Coordinated MOF. *ACS Appl. Nano Mater.* **2018**, *1*, 5408–5413. (c) Férey, G.; Mellot-Draznieks, C.; Serre, C.; Millange, F.; Dutour, J.; Surblé, S.; Margiolaki, I. A Chromium Terephthalate-Based Solid with Unusually Large Pore Volumes and Surface Area. *Science* **2005**, *309*, 2040–2042. (d) Banerjee, R.; Phan, A.; Wang, B.; Knobler, C.; Furukawa, H.; O’Keeffe, M.; Yaghi, O. M. High-Throughput Synthesis of Zeolitic Imidazolate Frameworks and Application to CO<sub>2</sub> Capture. *Science* **2008**, *319*, 939–943. (e) Furukawa, H.; Ko, N.; Go, Y. B.; Aratani, N.; Choi, S. B.; Choi, E.; Yazaydin, A. O.; Snurr, R. Q.; O’Keeffe, M.; Kim, J.; Yaghi, O. M. Ultra high Porosity in Metal-Organic Frameworks. *Science* **2010**, *329*, 424–428. (f) Kottlilil, D.; Gupta, M.; Tomar, K.; Zhou, F.; Vijayan, C.; Bhadraraj, P. K.; Ji, W. A cost-effective realization of multimode exciton-polaritons in single-crystalline microplates of a layered metal-organic framework. *ACS Appl. Mater. Interfaces* **2019**, *11*, 7288–7295. (g) Lu, W.; Wei, Z.; Gu, Z.-Y.; Liu, T.-F.; Park, J.; Park, J.; Tian, J.; Zhang, M.; Zhang, Q.; Gentle, T., III; Bosch, M.; Zhou, H.-C. Tuning the structure and function of metal–organic frameworks via linker design. *Chem. Soc. Rev.* **2014**, *43*, 5561–5593. (h) Stock, N.; Biswas, S. Synthesis of Metal-Organic Frameworks (MOFs): Routes to

- Various MOF Topologies, Morphologies, and Composites. *Chem. Rev.* **2012**, *112*, 933–969. (i) Li, M.; Li, D.; O’Keeffe, M.; Yaghi, O. M. Topological Analysis of Metal–Organic Frameworks with Polytopic Linkers and/or Multiple Building Units and the Minimal Transitivity Principle. *Chem. Rev.* **2014**, *114*, 1343–1370.
- (2) (a) Sun, D.; Ke, Y.; Mattox, T. M.; Parkin, S.; Zhou, H.-C. Stability and Porosity Enhancement through Concurrent Ligand Extension and Secondary Building Unit Stabilization. *Inorg. Chem.* **2006**, *45*, 7566–7568. (b) Horike, S.; Dincă, M.; Tamaki, K.; Long, J. R. Size-Selective Lewis Acid Catalysis in a Microporous Metal–Organic Framework with Exposed  $Mn^{2+}$  Coordination Sites. *J. Am. Chem. Soc.* **2008**, *130*, 5854–5855.
- (3) (a) Banerjee, R.; Furukawa, H.; Britt, D.; Knobler, C.; O’Keeffe, M.; Yaghi, O. M. Control of Pore Size and Functionality in Isoreticular Zeolitic Imidazolate Frameworks and their Carbon Dioxide Selective Capture Properties. *J. Am. Chem. Soc.* **2009**, *131*, 3875–3877. (b) Yang, Q.; Wiersum, A. D.; Llewellyn, P. L.; Guillermin, V.; Serre, C.; Maurin, G. Functionalizing porous zirconium terephthalate UiO-66(Zr) for natural gas upgrading: a computational exploration. *Chem. Commun.* **2011**, *47*, 9603–9605. (c) Gcwensa, N.; Chatterjee, N.; Oliver, C. L. Interchanged Hysteresis for Carbon Dioxide and Water Vapor Sorption in a Pair of Water-Stable, Breathing, Isoreticular, 2-Periodic, Zn(II)-Based Mixed-Ligand Metal–Organic Frameworks. *Inorg. Chem.* **2019**, *58*, 2080–2088.
- (4) (a) Cadiau, A.; Belmabkhout, Y.; Adil, K.; Bhatt, P. M.; Pillai, R. S.; Shkurenko, A.; Martineau-Corcus, C.; Maurin, G.; Eddaoudi, M. Hydrolytically stable fluorinated metal-organic frameworks for energy-efficient dehydration. *Science* **2017**, *356*, 731–735. (b) Gladys, J. A.; Curran, D. P.; Horváth, I. T. *Handbook of Fluorous Chemistry*; Wiley-VCH: Weinheim, Germany, 2004. (c) Horváth, I. T.; Rabai, J. Facile catalyst separation without water: fluorous biphasic hydroformylation of olefins. *Science* **1994**, *266*, 72–75. (d) Santra, A.; Senkovska, I.; Kaskel, S.; Bharadwaj, P. K. Gas Storage in a Partially Fluorinated Highly Stable Three-Dimensional Porous Metal–Organic Framework. *Inorg. Chem.* **2013**, *52*, 7358–7366.
- (5) Sharma, V.; De, D.; Saha, R.; Das, R.; Chattaraj, P. K.; Bharadwaj, P. K. A Cu(II)-MOF capable of fixing  $CO_2$  from air and showing high capacity  $H_2$  and  $CO_2$  adsorption. *Chem. Commun.* **2017**, *53*, 13371–13374.
- (6) (a) Gupta, M.; De, D.; Tomar, K.; Bharadwaj, P. K. From Zn(II) to Cu(II) Framework via Single-Crystal to Single-Crystal Metathesis with Superior Gas Uptake and Heterogeneous Catalytic Properties. *Inorg. Chim. Acta* **2018**, *482*, 925–934. (b) Gupta, A. K.; De, D.; Tomar, K.; Bharadwaj, P. K. A Cu(II) metal–organic framework with significant  $H_2$  and  $CO_2$  storage capacity and heterogeneous catalysis for the aerobic oxidative amination of  $C(sp^3)$ –H bonds and Biginelli reactions. *Dalton Trans.* **2018**, *47*, 1624–1634.
- (7) (a) Dietzel, P. D. C.; Johnsen, R. E.; Fjellvag, H.; Bordiga, S.; Groppo, E.; Chavan, S.; Blom, R. Adsorption properties and structure of  $CO_2$  adsorbed on open coordination sites of metal–organic framework  $Ni_2(dhpt)$  from gas adsorption, IR spectroscopy and X-ray diffraction. *Chem. Commun.* **2008**, 5125–5127. (b) McDonald, T. M.; D’Alessandro, D. M.; Krishna, R.; Long, J. R. Enhanced carbon dioxide capture upon incorporation of  $N,N'$ -dimethylethylenediamine in the metal–organic framework CuBTTri. *Chem. Sci.* **2011**, *2*, 2022–2028. (c) Vaidyanathan, R.; Iremonger, S. S.; Shimizu, G. K. H.; Boyd, P. G.; Alavi, S.; Woo, T. K. Direct Observation and Quantification of  $CO_2$  Binding Within an Amine-Functionalized Nanoporous Solid. *Science* **2010**, *330*, 650–653.
- (8) (a) Aguila, B.; Sun, Q.; Wang, X.; O’Rourke, E.; Al-Enizi, A. M.; Nafady, A.; Ma, S. Lower Activation Energy for Catalytic Reactions through Host–Guest Cooperation within Metal–Organic Frameworks. *Angew. Chem., Int. Ed.* **2018**, *57*, 10107–10111. (b) He, H.; Sun, Q.; Gao, W.; Perman, J. A.; Sun, F.; Zhu, G.; Aguila, B.; Forrest, K.; Space, B.; Ma, S. A Stable Metal–Organic Framework Featuring a Local Buffer Environment for Carbon Dioxide Fixation. *Angew. Chem., Int. Ed.* **2018**, *57*, 4657–4662. (c) Gao, W.-Y.; Chen, Y.; Niu, Y.; Williams, K.; Cash, L.; Perez, P. J.; Wojtas, L.; Cai, J.; Chen, Y.-S.; Ma, S. Crystal Engineering of an nbo Topology Metal–Organic Framework for Chemical Fixation of  $CO_2$  under Ambient Conditions. *Angew. Chem., Int. Ed.* **2014**, *53*, 2615–2619.
- (9) (a) Biggadike, K.; Angell, R. M.; Burgess, C. M.; Farrell, R. M.; Hancock, A. P.; Harker, A. J.; Irving, W. R.; Ioannou, C.; Procopiou, P. A.; Shaw, R. E.; Solanke, Y. E.; Singh, O. M. P.; Snowden, M. A.; Stubbs, R.; Walton, S.; Weston, H. E. Selective Plasma Hydrolysis of Glucocorticoid  $\gamma$ -Lactones and Cyclic Carbonates by the Enzyme Paraoxonase: An Ideal Plasma Inactivation Mechanism. *J. Med. Chem.* **2000**, *43*, 19–21. (b) Shaikh, A.-A. G.; Sivaram, S. Organic Carbonates. *Chem. Rev.* **1996**, *96*, 951–976.
- (10) (a) Clements, J. H. Reactive Applications of Cyclic Alkylene Carbonates. *Ind. Eng. Chem. Res.* **2003**, *42*, 663–674. (b) Lu, X. – B.; Darendbourg, D. J. Cobalt catalysts for the coupling of  $CO_2$  and epoxides to provide polycarbonates and cyclic carbonates. *Chem. Soc. Rev.* **2012**, *41*, 1462–1484. (c) Sakakura, T.; Choi, J.-C.; Yasuda, H. Transformation of Carbon Dioxide. *Chem. Rev.* **2007**, *107*, 2365–2387.
- (11) Robbe, Y.; Fernandez, J. P.; Dubief, R.; Chapat, J. P.; Sentenac-Roumanou, H.; Fatome, M.; Laval, J.-D.; Subra, G. Comparative radioprotective activity of various pentagonal compounds with two heteroatoms. *Eur. J. Med. Chem. Ther.* **1982**, *17*, 235–243.
- (12) (a) Belokon, Y. N.; Maleev, V. I.; North, M.; Usanov, D. L. VO(salen)(X) catalysed asymmetric cyanohydrin synthesis: an unexpected influence of the nature of anion X on the catalytic activity. *Chem. Commun.* **2006**, 4614–4616. (b) Motokuchō, S.; Sudo, A.; Sanda, F.; Endo, T. Controlled monomer insertion into polymer main chain: synthesis of sequence ordered polystyrene containing thiourethane and trithiocarbonate units by the RAFT process. *Chem. Commun.* **2002**, 1946–1947.
- (13) Runge, F.; El-Hewehi, Z.; Renner, H.-J.; Taeger, E. To note the trithiocarbonic acid. IV. The Preparation and Properties of Trithiocarbonic Diesters and Their Use as Pesticides. *J. Prakt. Chem.* **1960**, *11*, 284–308.
- (14) Spek, A. L. Single-crystal structure validation with the program PLATON. *J. Appl. Crystallogr.* **2003**, *36*, 7–13.
- (15) Chai, J. D.; Head-Gordon, M. Long-range corrected hybrid density functionals with damped atom–atom dispersion corrections. *Phys. Chem. Chem. Phys.* **2008**, *10*, 6615–6620.
- (16) Frisch, M. J.; et al. *Gaussian 09*, revision C.01; Gaussian, Inc.: Wallingford, CT, 2009.
- (17) Reed, A. E.; Weinstock, R. B.; Weinhold, F. Natural population analysis. *J. Chem. Phys.* **1985**, *83*, 735–746.
- (18) Wiberg, K. B. Application of the pople-santry-segal CNDO method to the cyclopropylcarbinyl and cyclobutylcation and to bicyclobutane. *Tetrahedron* **1968**, *24*, 1083–1096.
- (19) Reed, A. E.; Curtiss, L. A.; Weinhold, F. Intermolecular Interactions from a Natural Bond Orbital, Donor-Acceptor Viewpoint. *Chem. Rev.* **1988**, *88*, 899–926.
- (20) Glendening, E. D.; Reed, A. E.; Carpenter, J. E.; Weinhold, F. *NBO*, version 3.1; Gaussian Inc., Pittsburgh.
- (21) Mitoraj, M. P.; Michalak, A.; Ziegler, T. A. A Combined Charge and Energy Decomposition Scheme for Bond Analysis. *J. Chem. Theory Comput.* **2009**, *5*, 962–975.
- (22) Swart, M.; Solà, M.; Bickelhaupt, F. M. A new all-round density functional based on spin states and  $S_N2$  barriers. *J. Chem. Phys.* **2009**, *131*, 094103–1–094103–9.
- (23) Baerends, E. J.; et al. *ADF2013.01*, SCM, Theoretical Chemistry; SCM, Vrije Universiteit, Theoretical Chemistry: Amsterdam, The Netherlands, 2013.
- (24) te Velde, G.; Bickelhaupt, F. M.; Baerends, E. J.; Fonseca Guerra, C.; van Gisbergen, S. J. A.; Snijders, J. G.; Ziegler, T. Chemistry with ADF. *J. Comput. Chem.* **2001**, *22*, 931–967.
- (25) Bader, R. F. W. *Atoms in Molecules: A Quantum Theory*; Oxford University Press: Oxford, UK, 1990.
- (26) Lu, T.; Chen, F. W. Multiwfn: A multifunctional wavefunction analyzer. *J. Comput. Chem.* **2012**, *33*, 580–592.
- (27) Johnson, E. R.; Keinan, S.; Mori-Sanchez, P.; Contreras-Garcia, J.; Cohen, A. J.; Yang, W. Revealing Noncovalent Interactions. *J. Am. Chem. Soc.* **2010**, *132*, 6498–6506.

(28) Contreras-Garcia, J.; Johnson, E. R.; Keinan, S.; Chaudret, R.; Piquemal, J.-P.; Beratan, D. N.; Yang, W. NCIPLOT: A Program for Plotting Noncovalent Interaction Regions. *J. Chem. Theory Comput.* **2011**, *7*, 625–632.

(29) Humphrey, W.; Dalke, A.; Schulten, K. VMD: Visual molecular dynamics. *J. Mol. Graphics* **1996**, *14*, 33–38.

(30) De, D.; Pal, T. K.; Neogi, S.; Senthikumar, S.; Das, D.; Gupta, S. S.; Bharadwaj, P. K. A Versatile Cu<sup>II</sup> Metal–Organic Framework Exhibiting High Gas Storage Capacity with Selectivity for CO<sub>2</sub>: Conversion of CO<sub>2</sub> to Cyclic Carbonate and Other Catalytic Abilities. *Chem. - Eur. J.* **2016**, *22*, 3387–3396.

(31) De, D.; Neogi, S.; Bharadwaj, P. K. Stoichiometry Controlled Structural Variation in Three-Dimensional Zn(II)–Frameworks: Single-Crystal to Single-Crystal Transmetalation and Selective CO<sub>2</sub> Adsorption. *Cryst. Growth Des.* **2016**, *16*, 5238–5246.

(32) Fischer, M.; Hoffmann, F.; Fröba, M. Preferred Hydrogen Adsorption Sites in Various MOFs—A Comparative Computational Study. *ChemPhysChem* **2009**, *10*, 2647–2657.

(33) Rowsell, J. L. C.; Eckert, J.; Yaghi, O. M. Characterization of H<sub>2</sub> Binding Sites in Prototypical Metal–Organic Frameworks by Inelastic Neutron Scattering. *J. Am. Chem. Soc.* **2005**, *127*, 14904–14910.

(34) Saha, R.; Sharma, V.; De, D.; Bharadwaj, P. K.; Chattaraj, P. K. A (T-P) Phase Diagram for the Adsorption/Desorption of Carbon Dioxide and Hydrogen in a Cu(II)-MOF. *Polyhedron* **2018**, *153*, 254–260.

(35) (a) Cao, J.; Yu, M.; Li, H.; Wang, L.; Zhu, X.; Wang, G.; Shi, Y.; Cao, C. Synthesis of cyclic di- and trithiocarbonates from epoxides and carbon disulfide catalysed by N-heterocyclic carbene. *Res. Chem. Intermed.* **2015**, *41*, 5323–5330. (b) Beattie, C.; North, M. Titanium(salen)-Catalysed Synthesis of Di- and Trithiocarbonates from Epoxides and Carbon Disulfide. *ChemCatChem* **2014**, *6*, 1252–1259. (c) Beattie, C.; North, M. North, Mechanistic Investigation of the Reaction of Epoxides with Heterocumulenes Catalysed by a Bimetallic Aluminium Salen Complex. *Chem. - Eur. J.* **2014**, *20*, 8182–8188. (d) Diebler, J.; Spannenberg, A.; Werner, T. Atom economical synthesis of di- and trithiocarbonates by the lithium tert-butoxide catalyzed addition of carbon disulfide to epoxides and thiiranes. *Org. Biomol. Chem.* **2016**, *14*, 7480–7489. (e) Dotsenko, I. A.; Zhao, Q.; Franz, A. H.; Batoon, P.; Samoshina, N. M.; Samoshin, V. V. Convenient synthesis of 1,3-dithiolane-2-thiones: cyclic trithiocarbonates as conformational locks. *ARKIVOC* **2014**, *5*, 16–41.